

**OPEN ACCESS**

# Electrochemistry and Thermal Behavior of SiO<sub>x</sub> Made by Reactive Gas Milling

To cite this article: Yidan Cao *et al* 2020 *J. Electrochem. Soc.* **167** 110501

View the [article online](#) for updates and enhancements.



## ECS Membership = Connection

### ECS membership connects you to the electrochemical community:

- Facilitate your research and discovery through ECS meetings which convene scientists from around the world;
- Access professional support through your lifetime career;
- Open up mentorship opportunities across the stages of your career;
- Build relationships that nurture partnership, teamwork—and success!


**Join ECS!**

**Visit [electrochem.org/join](https://electrochem.org/join)**





# Electrochemistry and Thermal Behavior of SiO<sub>x</sub> Made by Reactive Gas Milling

Yidan Cao,<sup>1,2,z</sup> R. A. Dunlap,<sup>1,3,4</sup> and M. N. Obrovac<sup>1,2,3,\*;z</sup> 

<sup>1</sup>Department of Physics and Atmospheric Science, Dalhousie University, Halifax, Nova Scotia, Canada

<sup>2</sup>Department of Chemistry, Dalhousie University, Halifax, Nova Scotia, Canada

<sup>3</sup>Clean Technologies Research Institute, Dalhousie University, Halifax, Nova Scotia, Canada

<sup>4</sup>College of Sustainability, Dalhousie University, Halifax, Nova Scotia, Canada

SiO<sub>x</sub> with various oxygen contents were synthesized from Si powder by a simple room-temperature ball milling method by controlling the air exposure time during milling. The resulting SiO<sub>x</sub> consists of nano and amorphous Si dispersed in an amorphous silicon oxide matrix. The oxygen saturated composition of SiO<sub>0.37</sub> is thermally stable up to 800 °C and has improved cycling performance after annealing. The 1st irreversible capacity is reduced by high temperature annealing due to defect healing, while the high reversible capacity (1500–2000 mAh g<sup>-1</sup> or 1600–1800 Ah l<sup>-1</sup>) is well maintained. This work demonstrates the thermal properties of SiO<sub>x</sub> made by reactive gas milling and how internal defects directly influence its electrochemistry.

© 2020 The Author(s). Published on behalf of The Electrochemical Society by IOP Publishing Limited. This is an open access article distributed under the terms of the Creative Commons Attribution Non-Commercial No Derivatives 4.0 License (CC BY-NC-ND, <http://creativecommons.org/licenses/by-nc-nd/4.0/>), which permits non-commercial reuse, distribution, and reproduction in any medium, provided the original work is not changed in any way and is properly cited. For permission for commercial reuse, please email: [permissions@iopublishing.org](mailto:permissions@iopublishing.org). [DOI: 10.1149/1945-7111/ab9e83]



Manuscript submitted April 22, 2020; revised manuscript received June 12, 2020. Published June 30, 2020.

Supplementary material for this article is available [online](#)

With growing demands for high energy density storage devices, increasing the negative electrode capacity beyond what is possible with graphite has been widely studied in order to increase lithium ion battery (LIB) energy density.<sup>1–5</sup> In this vein, silicon and silicon-based intermetallic/composite negative electrode materials have been widely investigated due to silicon's high theoretical volumetric capacity of 2194 Ah l<sup>-1</sup>.<sup>6–8</sup> However, the alloying/de-alloying of Li with Si causes drastic volume changes (up to 280%), which can lead to particle/electrode mechanical failure, solid electrolyte interphase (SEI) disruption, electrolyte decomposition, and rapid capacity decay.<sup>9–11</sup> Extensive work has been carried out during the last two decades to address these problems. Improvements have been made by reducing the Si grain size,<sup>12</sup> controlling crystallization,<sup>9,10,13</sup> forming alloys/composites with other elements,<sup>14–16</sup> carbon coating,<sup>17,18</sup> etc. A great amount of effort is being applied to improve performance further.

SiO<sub>x</sub> has attracted much attention in recent years because of its high capacity, relatively long cycle life and special microstructure.<sup>19–24</sup> According to the random bonding model, SiO consists of nanometer regions of SiO<sub>2</sub> and nano-clusters of Si surrounded by a sub-oxide (SiO<sub>x</sub>) matrix.<sup>25</sup> This structure can be considered as a frozen non-equilibrium state. Commercial bulk amorphous silicon monoxide is produced by simultaneous evaporation of silicon and silicon dioxide (Si (s) + SiO<sub>2</sub>(s) → 2SiO(g)) in vacuum at approximately 1400 °C.<sup>25,26</sup> Other methods, including the thermal plasma (>5000 °C) process<sup>27</sup> and mechanical milling Si and amorphous SiO<sub>2</sub>,<sup>28</sup> have been reported for synthesizing SiO<sub>x</sub> powder. When used as an anode material in Li-ion cells, the low initial coulombic efficiency (ICE) of SiO is considered as one of its main drawbacks. The cause of this low ICE is the irreversible reaction of Li with oxygen in the suboxide matrix during the first cycle. Yamada et al. reported that the lithiation of SiO results in the formation of Li<sub>15</sub>Si<sub>4</sub>, surrounded by amorphous lithium silicon oxides, mainly Li<sub>4</sub>SiO<sub>4</sub>.<sup>29</sup> Small Si domain sizes in SiO can inhibit c-Li<sub>15</sub>Si<sub>4</sub> formation.<sup>30</sup> At cycling potentials typical for the anode in Li-ion cells (<0.9 V vs Li/Li<sup>+</sup>), the formation of Li<sub>4</sub>SiO<sub>4</sub> is irreversible and causes a decrease in ICE. This mechanism was verified by the study of SiO<sub>x</sub> (x = 0.11–0.67) and SiO<sub>x</sub> (x = 0.4, 0.7, 1.1, 1.3) thin films.<sup>21,31</sup>

Various methods have been proposed to improve the cycling performance and coulombic efficiency of SiO. Solid SiO is

thermodynamically unstable at high temperatures and disproportionates to Si and SiO<sub>2</sub> upon heating above 800 °C.<sup>32,33</sup> Nevertheless, high temperature heat treatment can increase SiO performance. The disproportionation of SiO at several temperatures was studied by C.M. Park et al., who found that a commercial SiO heat treated at 1000 °C contained well-developed Si nanocrystals uniformly dispersed within an amorphous SiO<sub>x</sub> matrix.<sup>33</sup> Coulombic efficiency and cycling performance were slightly increased after the heat treatment. Choi et al. found that controlling the microstructure in SiO could result in the application of strong compressive stresses to Si and thus improve ICE.<sup>34</sup> Carbon coating on SiO<sub>x</sub> particles is also effective for improving performance.<sup>33,35</sup> Carbon coating is usually carried out at high temperature (>800 °C) by using CVD,<sup>36–38</sup> hydrothermal carbonization,<sup>39,40</sup> or pyrolysis<sup>41–43</sup> methods. The high thermal stability of SiO<sub>x</sub> makes it amenable towards these processes.

Recently, we reported that amorphous SiO<sub>x</sub> (0 ≤ x ≤ 0.37) can be synthesized by simply ball milling Si in air.<sup>44</sup> This simple and low-cost synthesis method makes SiO<sub>0.37</sub> a highly attractive material because of its relatively low oxygen content, compared to conventionally made SiO. The lower the oxygen content of SiO<sub>x</sub>, the higher the reversible capacity and ICE. Here, a systematic study is presented, showing how the electrochemistry of SiO<sub>x</sub> is related to its microstructure as a function of oxygen content and heat treatment temperature. These results are compared to SiO<sub>x</sub> made by directly ball milling Si and SiO<sub>2</sub> together and also to a commercial SiO.

## Materials and Methods

**Materials synthesis.**—SiO<sub>x</sub> powders were synthesized by reactive gas ball milling according to the method described in Ref. 44. 0.5 ml of Si powder (Sigma Aldrich, –325 mesh, 99%) and 180 g of 0.125" stainless steel balls were placed in a 65 ml hardened steel vial equipped with an o-ring seal. The ball milling was conducted in either an air or argon atmosphere using a high energy ball mill (SPEX Model 8000-D, Spex CertiPrep, Metuchen, NJ). For argon milling, the milling vial was sealed in an Ar-filled glovebox with the o-ring seal in place. For air milling, the vial was clamped shut in air with the o-ring seal removed. A small hole was drilled in the clamping ring at the same level as the vial/cover interface to facilitate the entry of air during the milling process, as described in Ref. 44. All samples were ball milled for a total time of 20 h, but with different air exposure times during milling. Using this protocol,

\*Electrochemical Society Member.

<sup>z</sup>E-mail: [yidancoo@sz.tsinghua.edu.cn](mailto:yidancoo@sz.tsinghua.edu.cn); [mnobrovac@dal.ca](mailto:mnobrovac@dal.ca)

samples had 0–16 h of air exposure during milling. All samples were milled in argon for the final four hours of milling, in order to ensure the absorbed oxygen/activated oxygen species were fully reacted. The as-milled samples are labeled here by the number of hours of air milling. Some samples were subsequently heated for 3 h at 300 °C, 400 °C, 500 °C, 600 °C, 700 °C or 800 °C in an Ar atmosphere. For comparison, Si and SiO<sub>2</sub> (Sigma Aldrich, –325 mesh, 99%) powders were also ball milled together under Ar in either a 4:1 or 1:1 mole ratio. These samples are denoted as 4Si/SiO<sub>2</sub> and Si/SiO<sub>2</sub>, respectively. Commercial SiO (Sigma Aldrich, –325 mesh, 99%) and ball milled commercial SiO (4 h in Ar, BM-SiO) are used as reference.

**Characterization.**—X-ray diffraction (XRD) patterns were measured using a Rigaku Ultima IV diffractometer equipped with a Cu K $\alpha$  X-ray source and a graphite diffracted beam monochromator. Each XRD pattern was collected from 10° to 60°, 2-theta in 0.05° increments. The intensity of each phase and their grain sizes were measured by fitting the XRD patterns using Pseudo-Voigt peak functions. Bulk sample densities were measured with a He gas using a Micromeritics AccuPyc II 1340 gas pycnometer. Oxygen contents were determined by the LECO method (NSL Analytical Services, Inc., Cleveland OH). Specific surface area was determined by the single-point Brunauer–Emmett–Teller (BET) method using a Micromeritics Flowsorb I2300 surface area analyzer. Scanning electron microscope (SEM) images were measured using a TESCAN MIRA 3 IMU variable pressure Schottky field emission scanning electron microscope. X-ray photoelectron spectroscopy (XPS) measurements were conducted with a Multilab 2000 Multitechnique Surface Analysis Instrument (Thermo VG Scientific) using a non-monochromatic Al X-ray source (14 kV, 25 mA) and a chamber pressure of  $5 \times 10^{-9}$  torr. Sample powder was packed into a circular well (2 mm diameter  $\times$  2 mm depth) in a stainless-steel sample holder for the XPS measurement. Measurements were made with a pass energy of 30 eV and the analysis spot was approximately 0.6 mm in diameter. Some samples were sputter etched with an Ar-ion beam. XPS spectra at different etching depths were recorded successively after every etch period (1200 s). Transmission electron microscopy (TEM) images were taken using a Philips CM30 TEM. TEM specimens were made by suspending sample powders in methanol, sonicating 10 min, and placing a drop onto a lacey carbon coated TEM grid.

**Electrochemistry.**—Electrode slurries were prepared by mixing active materials, carbon black (Super C65, Imerys Graphite and Carbon) and a 10 weight % aqueous solution of lithium polyacrylate (LiPAA) (made by neutralizing a polyacrylic acid solution (Sigma-Aldrich, average molecular weight  $\sim$ 250,000 g mole<sup>-1</sup>, 35 wt% in H<sub>2</sub>O) with LiOH  $\cdot$  H<sub>2</sub>O (Sigma Aldrich, 98%) in distilled water) in distilled water to give a final solids volumetric ratio of 70/5/25 after drying. Slurries were mixed for one hour in a Retsch PM200 planetary mill at 100 rpm with three 13 mm tungsten carbide balls and then spread onto copper foil (Furukawa Electric, Japan) with a 0.004 inch gap coating bar. Then the coatings were dried in air for 1 h at 120 °C, cut into 1.3 cm disks and then heated under vacuum for 1 h at 120 °C with no further air exposure. The mass loadings of electrodes were  $1 \sim 2$  mg cm<sup>-2</sup>, which corresponds to an area specific capacity of  $2 \sim 2.5$  mAh cm<sup>-2</sup>.

Electrodes were assembled in 2325-type coin cells with a lithium foil counter/reference electrode. Two layers of Celgard 2300 separator were used in each coin cell. 1 M LiPF<sub>6</sub> (BASF) in a solution of ethylene carbonate, diethyl carbonate and monofluoroethylene carbonate (volume ratio 3:6:1, all from BASF) was used as electrolyte. Cell assembly was carried out in an Ar-filled glove box. Cells were cycled galvanostatically at  $30.0 \pm 0.1$  °C using a Maccor Series 4000 Automated Test System. For the 1st cycle, the electrodes were lithiated at a current of C/20 and held at 5 mV until the current decayed to a value of C/40 (trickle current), and delithiated at C/20 until a 0.9 V cutoff was reached. In subsequent

cycles, the electrodes were lithiated/delithiated at C/5 with a C/20 discharge trickle current (lithiation).

## Results

All SiO<sub>x</sub> products have a similar morphology, consisting of  $\sim$ 1  $\mu$ m particles, as observed by SEM (shown in our previous publication<sup>44</sup>). The BET surface area of all samples is also similar, being about  $21 \pm 1$  m<sup>2</sup> g<sup>-1</sup>. XRD patterns of SiO<sub>x</sub> powders made with different air exposure times are shown in Fig. 1a. The oxygen content of each sample is indicated. When Si is ball milled in Ar with the conditions used here, the steady-state result is a 2-phase mixture of  $\sim$ 7 nm nanocrystalline Si (n-Si) and amorphous Si (a-Si).<sup>45</sup> If the sample is exposed to air during milling, the n-Si fraction decreases, while the a-Si fraction increases, and an amorphous SiO<sub>2- $\delta$</sub>  phase is formed, causing additional intensity to appear left of the Si (111) peak at 28.5°. A steady state is reached at 8 h of milling time. At this point the n-Si fraction is nearly consumed and the oxygen content is about  $x = 0.37$ . Neither the grain structure nor oxygen content changes with further air milling time, as shown in Fig. S1 (available online at [stacks.iop.org/JES/167/110501/mmedia](https://stacks.iop.org/JES/167/110501/mmedia)). Also shown in Fig. 1a for comparison are the XRD patterns of ball milled commercial SiO (BM-SiO) and a 4:1 by mole sample of Si and SiO<sub>2</sub> ball milled in Ar (4Si/SiO<sub>2</sub>), which has a similar composition (SiO<sub>0.4</sub>) to the oxygen saturated ball milled SiO<sub>x</sub> samples (SiO<sub>0.37</sub>). Compared to the Si(16h) sample, there is more X-ray intensity from silicon oxide in BM-SiO, due to its higher oxygen content. In addition, there is significant amount of FeSi contamination in the BM-SiO sample, compared to the Si(16h) sample. The 4Si/SiO<sub>2</sub> sample diffraction pattern is also similar to that of Si(16h). However, a small Fe peak at  $\sim$ 44.7° is also present in this sample, as indicated by a red arrow in Fig. 1a. The iron contamination in these samples arises from the steel ball mill vial and milling media and reflects the high abrasiveness of SiO<sub>2</sub> and SiO. The Fe contamination becomes more pronounced after high temperature heating, as shown in Fig. S5d for the 4Si/SiO<sub>2</sub> sample, where impurity peaks from Fe and FeSi are apparent. In contrast, no obvious Fe contamination is observed in the samples made by ball milling Si in air.

Figure 1b shows XPS Si 2p spectra of ball milled SiO<sub>x</sub> samples. The XPS Si 2p spectrum of Si(0h) consists of a peak corresponding to elemental Si and another peak corresponding to Si<sup>4+</sup>. These peaks correspond to bulk Si and surface Si oxides or hydroxides, respectively. As the amount of air exposure time during milling increases, the Si<sup>4+</sup> peak grows, as would be expected for the formation of SiO<sub>2</sub>-like species. The XPS spectra do not change appreciably after 8 h of air exposure during milling, in agreement with the oxygen content and XRD analyses, which show that these samples reach a steady-state structure and oxygen content after 8 h milling in air. BM-SiO, whose composition is SiO<sub>0.97</sub>, has a higher oxygen content and, accordingly, more silicon exists as Si<sup>4+</sup> as detected by XPS. Figures 1c and 1d show depth profile Si(4h) and Si(8h) XPS Si 2p spectra. The Si<sup>4+</sup> content decreases gradually with prolonged etching time in Si(4h). In Si(8h), the Si<sup>4+</sup> content inside the sample is relatively stable, except that there is more Si<sup>4+</sup> on the surface. This suggests that the reaction between Si and air proceeds from the surface and a steady-state is reached after 8 h, which is consistent with the reported mechanism.<sup>44</sup> Figure S2a shows the O 1s XPS spectra of all samples. There is no significant difference of the oxygen state in all the samples except in Si(0h), which may be related to rich hydroxide groups on the surface of Si(0h). Depth profile Si(4h) and Si(8h) XPS O 1s spectra shown in Figs. S2b and S2c show that oxygen state in the samples are homogeneous, indicating that the reaction between silicon and oxygen only produce one kind of uniformly distributed oxygen species.

We have reported the electrochemistry of SiO<sub>x</sub> samples previously.<sup>44</sup> Here, we show that the features in the potential profiles are directly related to the oxygen content. Potential profiles and

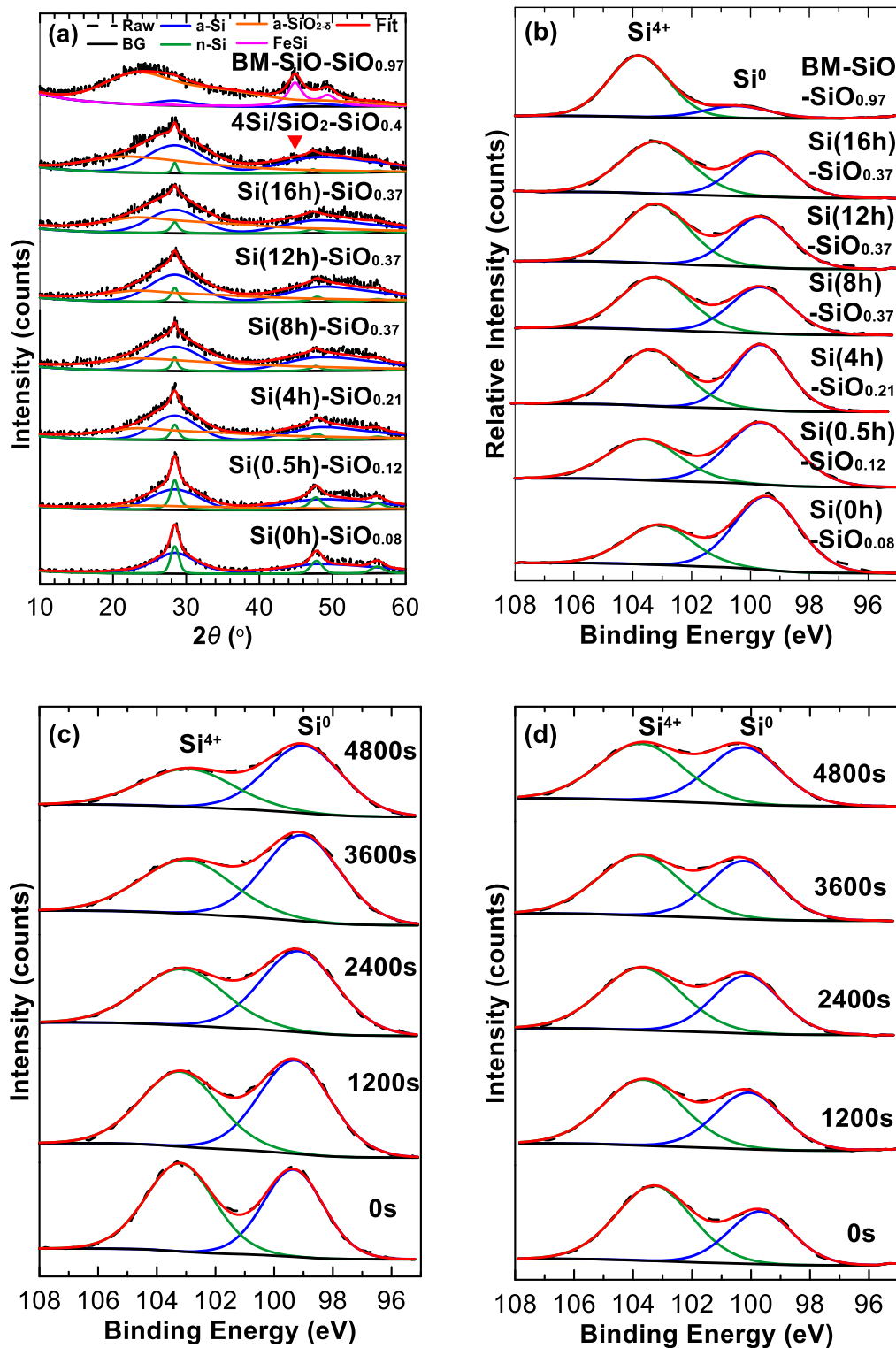


**Figure 1.** (a) X-ray diffraction pattern fitting results of  $\text{SiO}_x$  samples, ball milled  $\text{Si}+\text{SiO}_2$  (4Si/SiO<sub>2</sub>) and ball milled commercial SiO (BM-SiO), (b) XPS Si 2p spectra of  $\text{SiO}_x$  samples and BM-SiO. Depth XPS Si 2p spectra of (c) Si(4h)-SiO<sub>0.21</sub>, (d) Si(8h)-SiO<sub>0.37</sub>. The compositions of each sample are indicated in figures.

differential capacity curves of all samples are shown in Figs. 2a and 2b. The capacity of the  $\text{SiO}_x$  samples decreases with increasing air exposure time during milling, reflecting the reduced amount of elemental silicon present in  $\text{SiO}_x$  as the oxygen content is increased. A high potential first lithiation plateau at about 0.5 V is present for  $\text{SiO}_x$  electrodes with air exposure time longer than 4 h during milling. Similar high potential first lithiation plateaus are observed for 4Si/SiO<sub>2</sub> and BM-SiO electrodes, except these appear at even higher

potentials (0.63 V for 4Si/SiO<sub>2</sub>, 0.77 V for BM-SiO). After the first lithiation, this high potential plateau is no longer present and all of the potential profiles have the characteristic lithiation/delithiation features of amorphous silicon,<sup>9</sup> indicating that silicon is the only active phase present. In a previous study, we showed that the capacity associated with the high potential first lithiation plateau increases in area with air exposure time during milling for the  $\text{SiO}_x$  samples, consistent with the irreversible formation of a  $\text{Li}_4\text{SiO}_4$



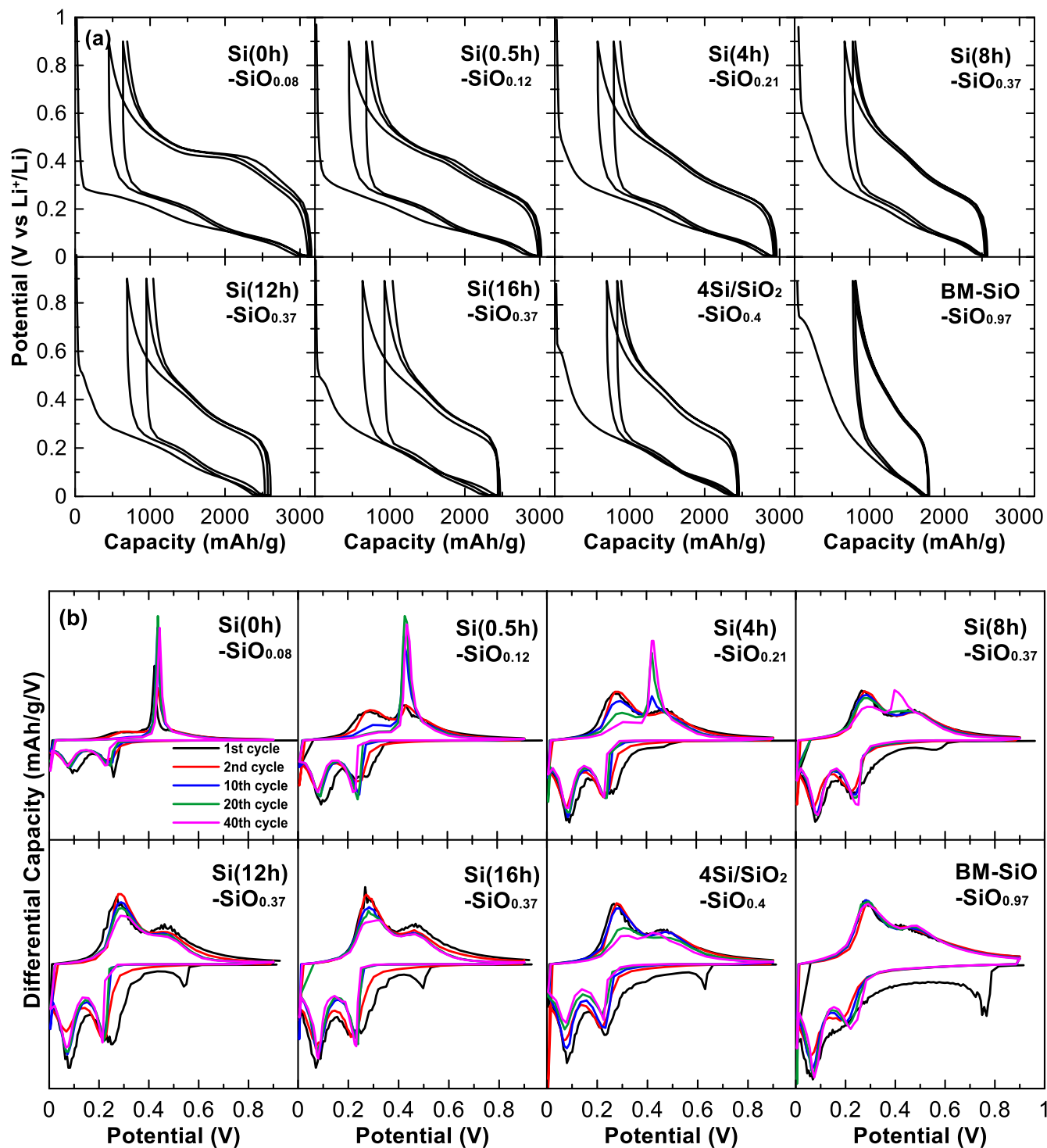


**Figure 2.** Electrochemical performance of the SiO<sub>x</sub> electrodes. (a) Potential vs capacity curves, (b) differential capacity curves.

matrix.<sup>44</sup> Here we observe that the potential of this plateau also increases linearly with increasing oxygen content, as shown in Fig. S3. This may be due to an increased electron density on oxygen or weaker Si-O bonds as the oxygen concentration is increased, facilitating reaction with Li at higher potentials. This will be discussed in greater detail in relation to annealed samples below.

A delithiation plateau at about 0.43 V in the potential profiles of the SiO<sub>x</sub> samples, shown in Fig. 2a, and a corresponding peak in their differential capacity, shown in Fig. 2b, indicates the delithiation of Li<sub>15</sub>Si<sub>4</sub> phase, which would have been formed below 50 mV during the previous lithiation half-cycle. With increasing air

exposure time during milling, the formation of Li<sub>15</sub>Si<sub>4</sub> is reduced gradually. For Si(0.5h), Si(4h) and Si(8h), Li<sub>15</sub>Si<sub>4</sub> formation is fully suppressed during initial cycles. As the oxygen exposure time is increased further to 12 h, the formation of Li<sub>15</sub>Si<sub>4</sub> is completely suppressed for all 50 cycles and little change is seen in the differential capacity curve. When the oxygen content exceeds  $x = 0.2$ , i.e. Si(4h), the differential capacity curves in Fig. 2b exhibit a tail during delithiation corresponding to additional capacity that extends to potentials higher than 0.9 V. The magnitude of this tail increases as the oxygen content is increased. Therefore, all the electrodes were delithiated to 2.5 V to further understand this

process. Figure S4a shows the potential profiles of  $\text{SiO}_x$  alloys cycled between 5 mV and 2.5 V. Corresponding differential capacity curves are shown in Fig. S4b in the 0.8–2.5 V range. Substantial delithiation capacity can be obtained above 0.9 V for all compositions. This high potential capacity has been associated with lithium delithiation from  $\text{Li}_4\text{SiO}_4$ ,<sup>21</sup> and is quantified below.

Figures 3a and 3b show the lithiation and delithiation capacities of the electrodes. A model suggested by Al-Maghrabi et al. for the cycling behavior of sputtered Si–O alloy thin films (Ref. 21) was used to describe the results. This model assumes that active Si and  $\text{Li}_4\text{SiO}_4$  are formed during the first lithiation of Si–O alloys, where

the Si formed has a reversible capacity of 3.75 li per Si and the  $\text{Li}_4\text{SiO}_4$  is inactive below 0.9 V during delithiation. Figure 3a shows that the first lithiation capacity decreases with increasing oxygen content, as well predicted by this model. Figure 3b shows the reversible (first delithiation) specific capacity for cells cycled up to 0.9 V and 2.5 V. The cells cycled up to 2.5 V have slightly higher reversible capacity than the cells cycled to 0.9 V because of the extra capacity observed in that region of the potential profiles (shown in Fig. S4a). The reversible capacities are below that predicted by the model and all deviations from the model are nearly the same. Furthermore, this is true even for the  $\text{SiO}_{0.1}$  sample, that is nearly

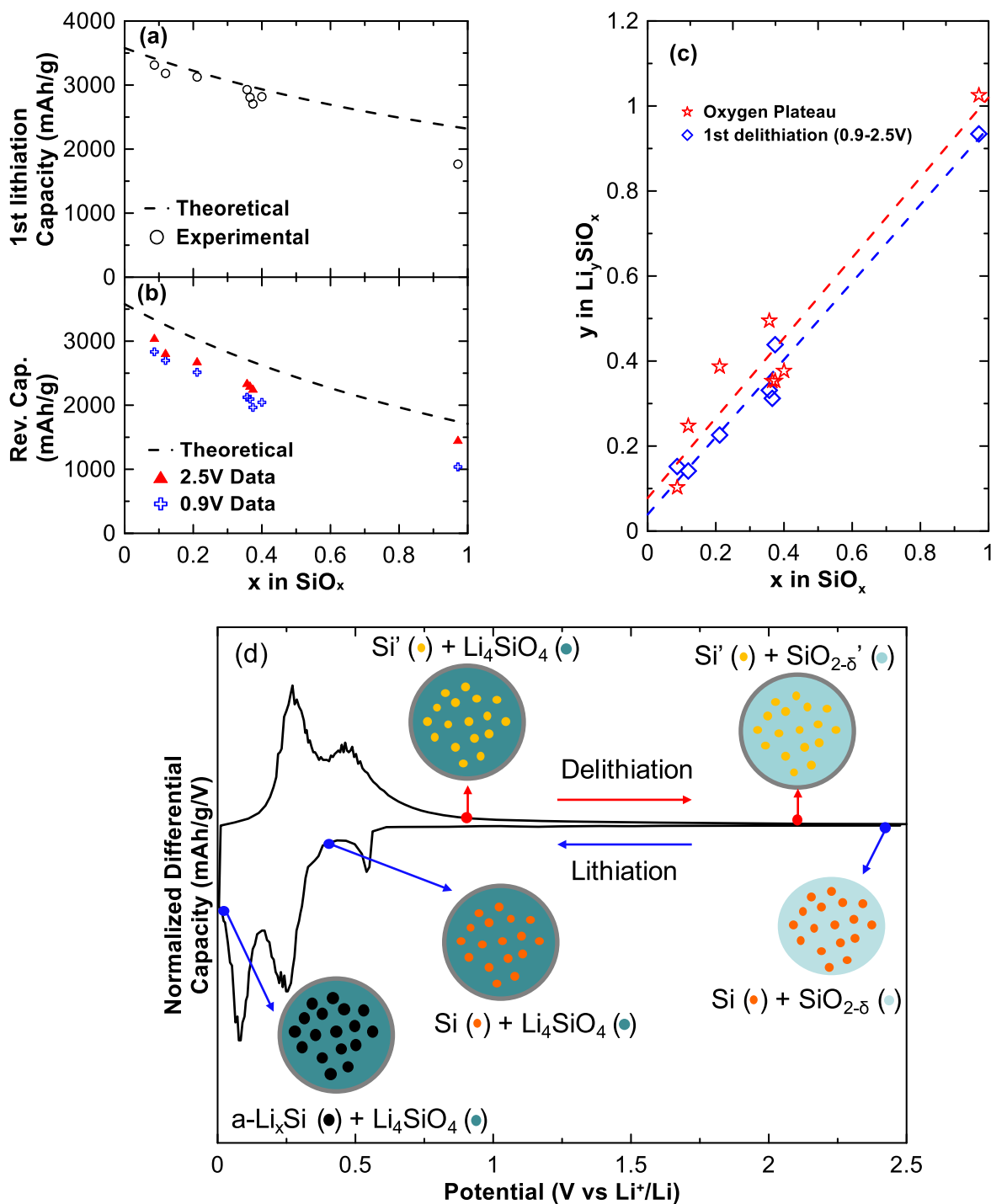


**Figure 3.** (a) First discharge capacity for  $\text{SiO}_x$  electrodes. (b) Reversible capacity (first charge) to 0.9 V (black circles) and 2.5 V (red triangles) as a function of  $x$  in  $\text{SiO}_x$ . (c) The amount of Li inserted per mole of  $\text{SiO}_x$  at different states. Red stars: 1st lithiation high potential plateau. Blue diamonds: the difference in delithiation capacity between electrodes cycled up to 0.9 V and 2.5 V, respectively. (d) Lithiation/delithiation process in a typical  $\text{SiO}_x$  particle.

pure Si. This suggests that a systematic reduction in capacity is occurring that is not related to the alloy chemistry. We believe that this systematic capacity loss is due to the mechanical disconnection of the alloy from the electrodes during delithiation as the alloy undergoes volume contraction, which is commonly observed for high capacity alloys, especially in coatings that do not contain graphite.<sup>15</sup>

Figure 3c shows the amounts of lithium associated with the high potential initial lithiation plateau and the first 0.9–2.5 V delithiation capacity plotted vs  $x$  in  $\text{SiO}_x$ . Both quantities increase linearly with the oxygen content, with slopes of 0.95 and 0.92, which are nearly equal to one lithium per oxygen. This indicates that the high potential initial lithiation plateau and the first delithiation capacity above 0.9 V are both correlated with the oxygen content in  $\text{SiO}_x$ . Moreover, the slope of  $\text{Li}/\text{O} \approx 1$ , is consistent with the formation of  $\text{Li}_4\text{SiO}_4$  during the initial high potential lithiation plateau and the full delithiation of  $\text{Li}_4\text{SiO}_4$  in the potential range of 0.9–2.5 V. This is consistent with the first lithiation and delithiation capacity predictions shown in Figs. 3a and 3b, which also support the formation of  $\text{Li}_4\text{SiO}_4$ .

The scheme of the lithiation/delithiation process in a typical  $\text{SiO}_x$  electrode is summarized in Fig. 3d. Initially the  $\text{SiO}_x$  particles consist of isolated nano-Si embedded in a  $\text{SiO}_{2-\delta}$  matrix (see XRD, and TEM results below). The  $\text{SiO}_{2-\delta}$  phase is first lithiated at the potential indicated by the first lithiation peak above 0.5 V. At potentials just below this peak, the sample is composed of nano-Si embedded in a  $\text{Li}_4\text{SiO}_4$  matrix. At lower potentials the nano-Si phase is lithiated.  $\text{Li}_{15}\text{Si}_4$  formation is fully suppressed during lithiation, so that only broad peaks corresponding to the delithiation of a- $\text{Li}_x\text{Si}$  are present in the differential capacity curve during delithiation. At potentials higher than 0.9 V, lithium is removed from the  $\text{Li}_4\text{SiO}_4$  phase.

The  $\text{SiO}_x$  materials were annealed at high temperatures to test their thermal stability and study the dependence of microstructure and electrochemistry on temperature. Figure 4a shows changes in the XRD pattern of the Si(8h) sample after heating to different temperatures up to 800 °C. At 800 °C, the (111) Si XRD peak at 28° consists of a single narrow peak, corresponding to an average crystallite size of 7 nm (the broad intensity towards lower angles, corresponds to amorphous  $\text{SiO}_{2-\delta}$ ). At lower temperatures, the Si (111) peak seems to be a combination of the peak from ~7 nm n-Si grains with broader peaks from smaller a-Si grains, which are X-ray

amorphous. Therefore, to quantify changes in the microstructure during heating, the XRD patterns were fit using a polynomial background and pseudo-Voigt peak shape functions representing nanocrystalline Si, X-ray amorphous Si, and amorphous  $\text{SiO}_{2-\delta}$ . This interpretation of the grain structure will be justified from TEM observations below. The nanocrystalline-Si/amorphous-Si (n-Si/a-Si) fraction was calculated from the fits and is plotted in Fig. 4b as a function of heating temperature. Also shown in the plot is sample oxygen content from LECO testing. The fraction of n-Si in the samples remains low at temperatures less than 700 °C. Significant crystallization occurs when the annealing temperature is higher than 700 °C. Figure 4b also shows that the oxygen content does not change with annealing temperature even when the sample is heated up to 800 °C.

Figures S5a–S5c shows XRD patterns of all the  $\text{SiO}_x$  powders, as milled, and after heating to 600 °C and 800 °C. After annealing, a higher fraction of n-Si is formed, especially for materials annealed at 800 °C, and especially for those materials ball milled for brief times in air. The size of the Si crystallites was about 7 nm for all samples annealed at 800 °C, i.e.: irrespective of air exposure time during milling or annealing conditions. These XRD patterns were fitted as a combination of a-Si, n-Si and amorphous  $\text{SiO}_{2-\delta}$  peaks, as described above and the n-Si/a-Si ratio is plotted in Fig. 4c as a function of air exposure time during milling. At 600 °C, only slight increases in the amount of nanocrystalline Si phase are observed for those samples milled in air for less than 4 h. At 800 °C, significant crystallization occurs in the Si(Oh) sample. As the air exposure time during milling is increased, the tendency for Si to crystallize during annealing is drastically reduced and reaches a steady state after the sample reaches its oxygen saturation point, i.e. after 8 h air exposure time during milling. For these samples, about 55% of the Si remains amorphous, even after heating to 800 °C. Figure S1 shows the oxygen content of  $\text{SiO}_x$  materials with different air exposure times during milling and for the same materials after annealing at high temperatures. The oxygen contents after annealing these materials at 600 °C and 800 °C are similar to the corresponding room-temperature samples. Therefore, no oxygen loss occurs during heating these samples in argon up to 800 °C.

Figure 5 shows TEM images of Si(8h) annealed at various temperatures. The materials are mostly amorphous, but a small amount of <10 nm embedded grains, which correspond to n-Si, can be observed. The n-Si grains are completely isolated from one

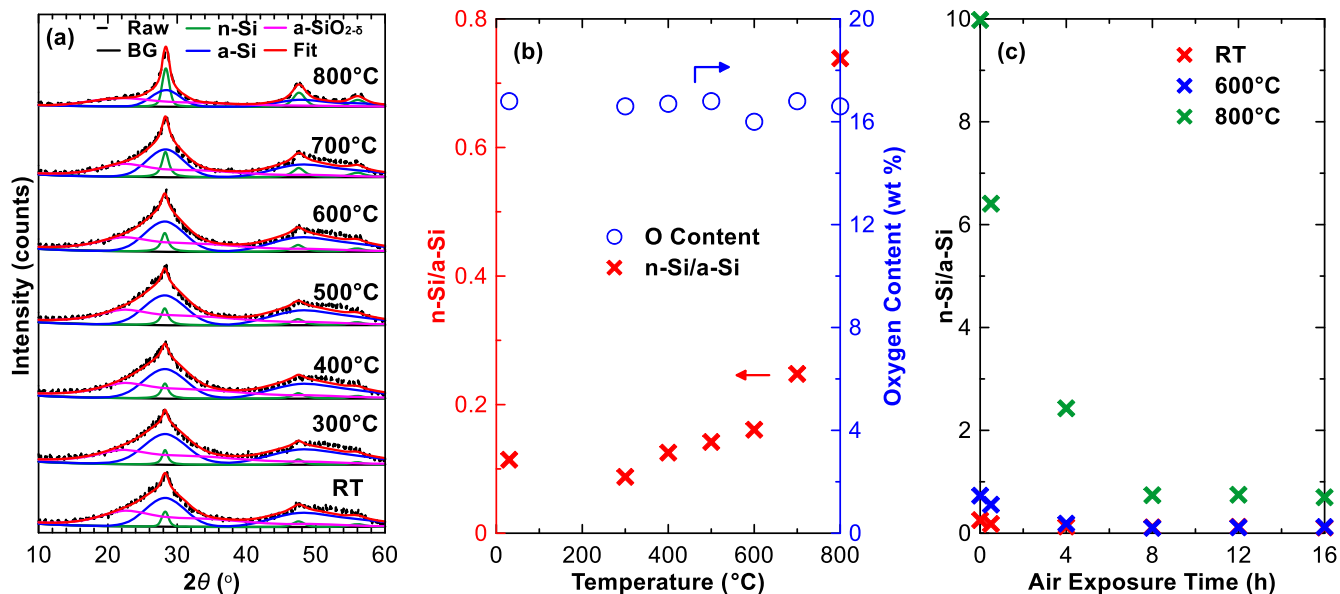


**Figure 4.** (a) Dependence of the nanocrystalline-Si/amorphous-Si (n-Si/a-Si) phase ratio on sample air exposure time, (b) XRD profiles of Si(8h)- $\text{SiO}_{0.37}$  samples annealed at various temperatures, (c) Dependence of the oxygen content, and nanocrystalline-Si/amorphous-Si (n-Si/a-Si) phase ratio on annealing temperature.

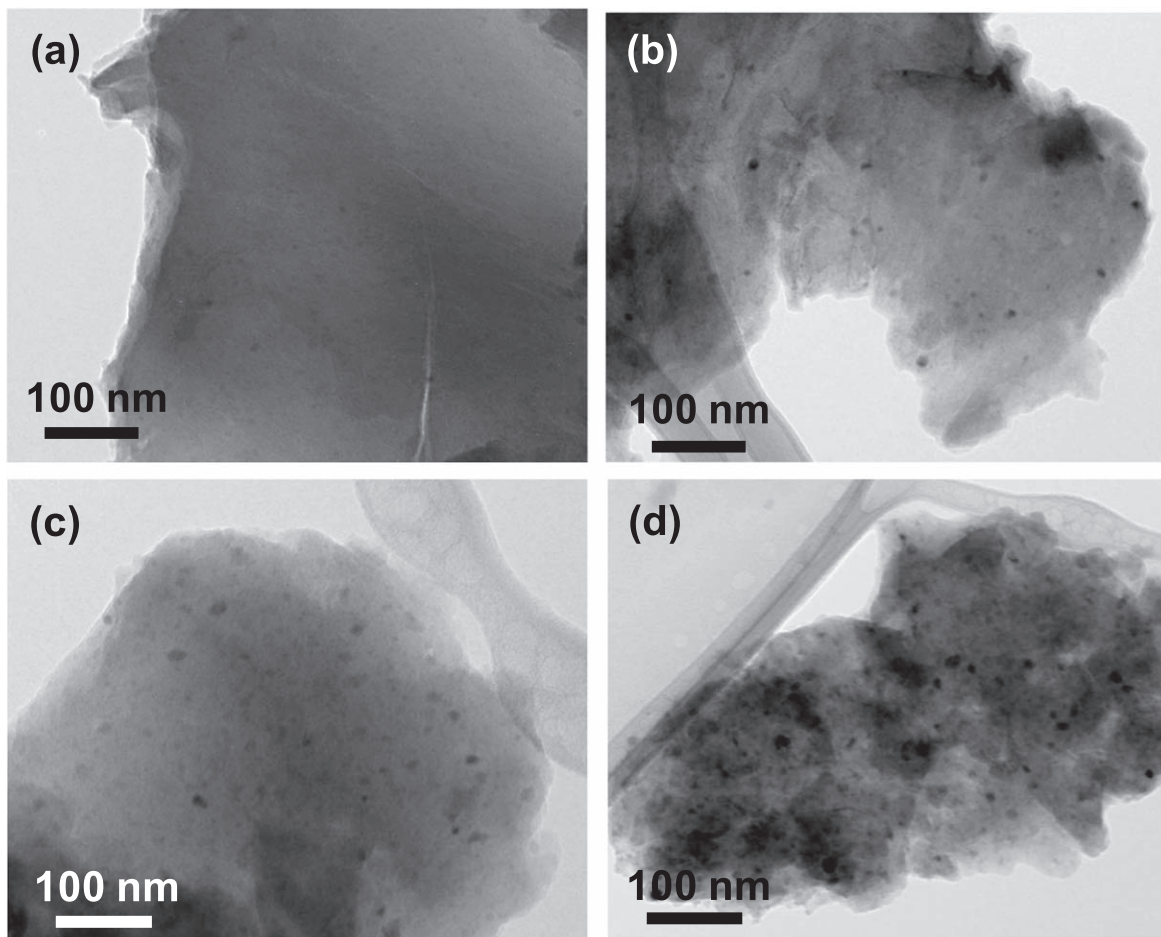


**Figure 5.** TEM images of (a) RT synthesized, (b) 400 °C annealed, (c) 600 °C annealed, and (d) 800 °C annealed Si(8h)-SiO<sub>0.37</sub> samples.

another and are surrounded by an amorphous phase. The amount and average size of silicon grains increases with annealing temperature. This indicates that the crystallization of silicon in the samples are formed through nucleation and aggregation. However, the aggregates appear to still be well separated and their maximum size does not exceed ~5–10 nm. The surrounding matrix likely impedes aggregation, limiting the Si grain size during annealing. These observations are consistent with the XRD results above.

To summarize these results, the SiO<sub>x</sub> materials made by milling Si in air are composed of grains of n-Si that are about 7 nm in size and a-Si dispersed in an amorphous SiO<sub>2-δ</sub> matrix. During heating to 800 °C no oxygen loss occurs, and the size of the n-Si phase does not change appreciably. Instead, the amount of n-Si grains increases and the amount of a-Si decreases. However, the Si phase cannot crystallize beyond 10 nm in size, indicating that ≤10 nm regions of active Si must be isolated from each other by the SiO<sub>2-δ</sub> matrix. Such a microstructure is highly desirable, since the active Si phase should be well protected from reaction with electrolyte from the surrounding amorphous matrix phase. What's more, since active Si nanoregions are completely isolated by the amorphous matrix phase, Si aggregation during cycling or during high temperature treatment should be limited, resulting in good capacity retention and high thermal stability.

For comparison 4Si/SiO<sub>2</sub> and Si/SiO<sub>2</sub> samples were also annealed at 600 °C. Figure S5d shows XRD patterns of these samples before and after annealing. The 4Si/SiO<sub>2</sub> sample has a composition and XRD pattern that is similar to the Si(8h), excepting a small peak from Fe contamination is present. The Si/SiO<sub>2</sub> sample has a composition that is similar to the SiO sample; however, its XRD pattern shows extensive Fe contamination. After heating the 4Si/SiO<sub>2</sub> and Si/SiO<sub>2</sub> samples, peaks from Fe contamination become

sharper and more pronounced. Therefore, ball milling Si and SiO<sub>2</sub> directly can result in a similar composition as ball milling Si in air, but a higher level of Fe contamination results. This is likely because of the abrasive nature of SiO<sub>2</sub> precursor prior to its being incorporated in the alloy.

Si 2p and O 1s XPS spectra were measured to characterize the state of silicon and oxygen in the samples annealed at different temperatures. As shown in Fig. S6a, the Si 2p XPS spectra of the Si (8h) sample consist of a peak corresponding to elemental Si and another peak corresponding to Si<sup>4+</sup>. The content of elemental Si on the surface slightly increases after heating. However, the O 1s and Si 2p surface XPS spectra do not change appreciably after the sample was annealed at different temperatures, except for a slight shift towards higher binding energies at 800 °C, which may be from the conversion of hydroxide surface groups into oxide groups. In order to better understand the states of oxygen and silicon species, XPS spectra at different depths were probed by argon ion etching unheated and heated Si(8h) samples and the results are shown in Fig. 6. As shown in Fig. 6a, the O 1s peak shifts only very slightly towards higher binding energies with detection depth in the unheated sample. This shift may be from the presence of hydroxide species on the surface. In contrast, a second higher binding energy (BE) O 1s peak, which is related to more stable oxygen species, is present in the sample annealed at 800 °C when the sample is etched for some time. As shown by the LECO test results in Fig. 4b, the oxygen content does not change with annealing temperature. Therefore, the increasing O 1s BE in the bulk is due to the increasing amount of more stable oxygen species. Figure 6b shows the Si 2p XPS depth profiles of the Si(8h) sample as synthesized and after the sample was heated at 800 °C. The Si<sup>4+</sup>/Si<sup>0</sup> ratio is highest on the surface and



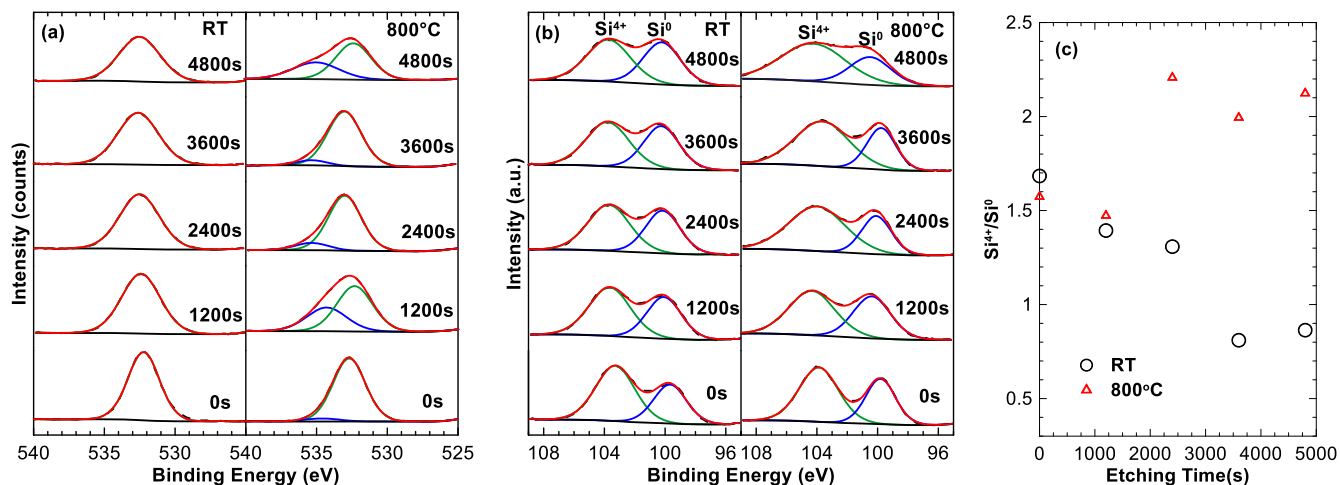


**Figure 6.** Depth XPS profiles of the Si(8h)-SiO<sub>0.37</sub> sample as synthesized at room temperature (RT) and after annealing at 800 °C (a) O 1s (b) Si 2p. (c) Correlation between Si<sup>4+</sup>/Si<sup>0</sup> ratios and etching time.

decreases with greater depth in the room temperature synthesized sample, as shown in Fig. 6c. Si<sup>4+</sup>/Si<sup>0</sup> ratios in the bulk are increased in the 800 °C annealed sample while the surface silicon state is similar to the room-temperature sample. It has been reported that solid SiO is thermodynamically unstable towards disproportionation into Si and SiO<sub>2</sub> at high temperatures.<sup>33</sup> The above results indicate that the silicon suboxide (SiO<sub>2- $\delta$</sub> ) may undergo disproportionation by forming silicon- and silicon-dioxide-like regions in the synthesized SiO<sub>x</sub>.

Potential profiles of all electrodes are shown in Fig. S7. During the first lithiation of the room temperature synthesized alloys, the high potential plateau at about 0.5 V increases in capacity with increasing oxygen content, as discussed above and in Ref. 44. Figures S7b and S7c show potential profiles of the same samples after annealing at 600 °C and 800 °C, respectively. The oxygen related high potential lithiation

plateau at 0.5 V becomes less pronounced after annealing at high temperatures. Moreover, the plateau position shifts to lower potential with increasing annealing temperature. Corresponding differential capacity curves of the electrodes in Fig. S7 are shown in Fig. S8. Corresponding to the trends seen in the potential profiles, the peak corresponding to the high potential initial lithiation plateau increases in potential and area with oxygen content and decreases in potential and area with annealing temperature. During delithiation, a peak due to Li<sub>15</sub>Si<sub>4</sub> delithiation is prominent for samples with low air milling time and/or high heating temperature. After annealing at 800 °C, sharp Li<sub>15</sub>Si<sub>4</sub> peaks are present in all samples. The increase in Li<sub>15</sub>Si<sub>4</sub> formation is related to the increasing crystalline silicon content, as shown in the XRD and TEM results.

Figure 7a shows the differential capacity curves of the 1st lithiation process of the Si(8h) sample after heating to different

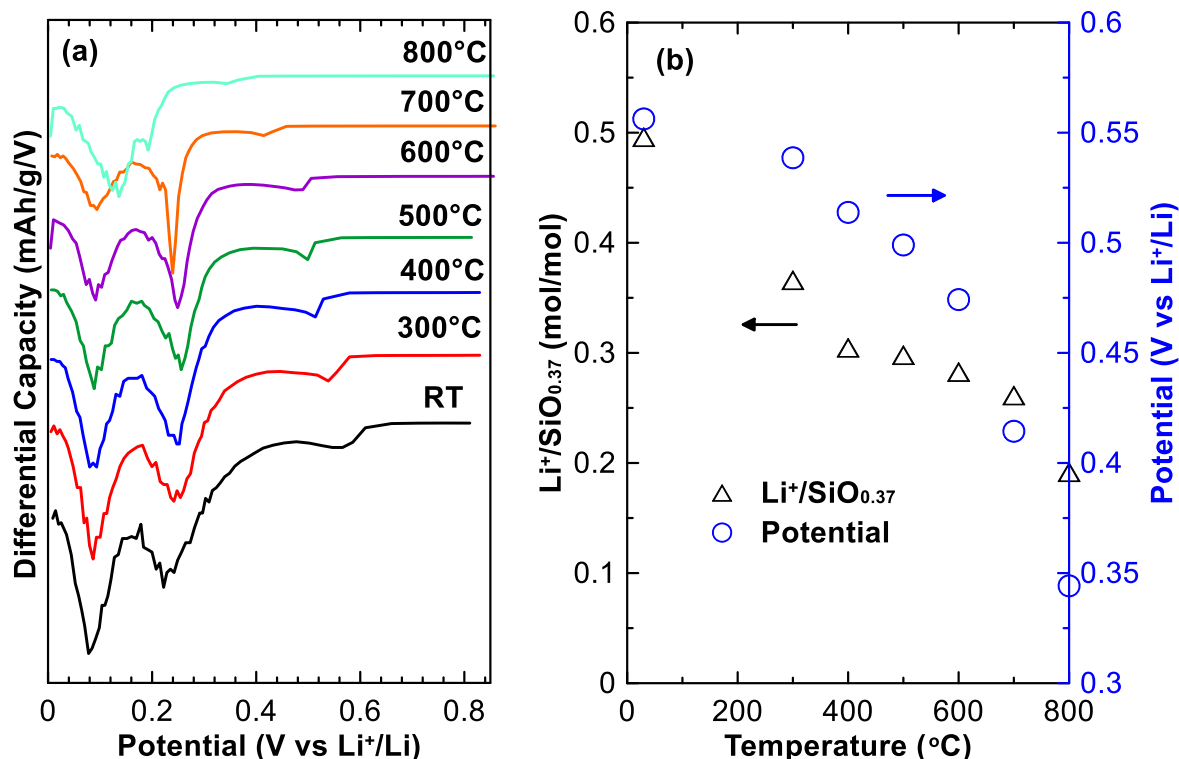


**Figure 7.** (a) Differential capacity curves of first lithiation, (b) Oxygen related lithiation peak potential and amount of lithium inserted per mole of Si(8h)-SiO<sub>0.37</sub> annealed at different temperatures.

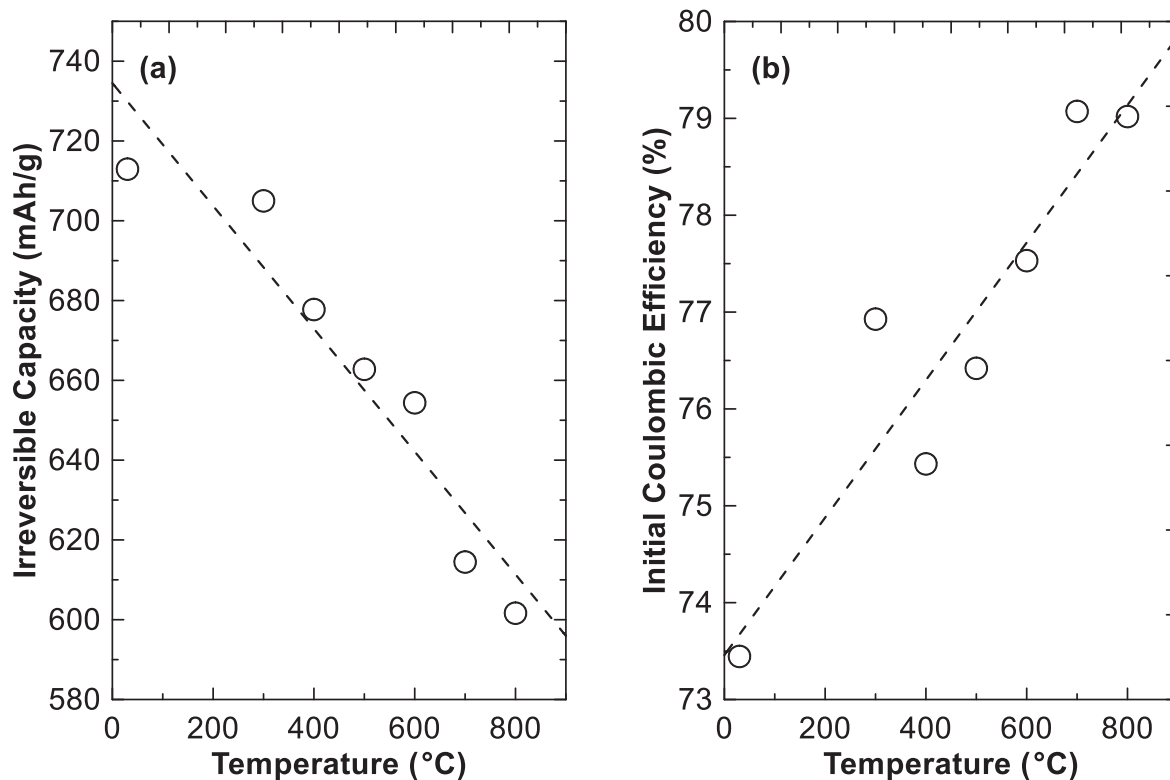


**Figure 8.** Correlation between initial irreversible capacity (a), ICE (b) and annealing temperatures of Si(8h)-SiO<sub>0.37</sub>.

temperatures. All potential profiles and differential capacity curves are shown in Fig. S9. The high potential initial lithiation peak is present at  $\sim 0.55$  V in the RT sample, and shifts to lower potential and decreases in area with increasing annealing temperature. The potential and area of this peak are plotted in Fig. 7b. With increasing annealing temperature, potential decreases linearly and the amount of Li associated with this potential plateau also decreases roughly linearly. This plateau is directly related to the irreversible reaction of Li with reactive oxygen that is easily available for reaction. LECO testing shows that there is no change of oxygen content in the annealed samples (Figs. S1, 4b). Therefore, the oxygen bonding environment must be changing. This is supported by XPS results, which show that higher bonding energy electrons are associated with oxygen after heating (Fig. 6a). We therefore ascribe the initial high potential oxygen peak to oxygen near defect sites that can react with lithium at high potential. Heating allows defect oxygen to form stronger bonds and eliminates some defect sites, resulting in the reduction in the potential and capacity of the initial high potential lithiation plateau. To confirm this result further, cells were constructed of commercial SiO, commercial SiO after ball milling, and commercial SiO after ball milling and annealing. The differential capacity curves are shown in Fig. S10. No initial high potential lithiation plateau is observed in the commercial SiO sample (Fig. S10a). After introducing defects by ball milling, the plateau appears (Fig. S10b), and after annealing to reduce oxygen defects, the plateau disappears (Figs. S10d, S10f).

The first cycle irreversible capacity, which is related to the irreversible lithiation reaction between lithium and silicon oxide, is reduced after annealing, as shown for Si(8h)-SiO<sub>0.37</sub> samples in Fig. 8a. This indicates that annealing not only heals oxygen defect sites, but also reduces the amount of reactive oxygen sites that can react with lithium during lithiation. Figure 8b shows that the initial coulombic efficiency (ICE) of SiO<sub>x</sub> is increased from  $\sim 73\%$  to  $\sim 79\%$  as the annealing temperature is increased. The increase in ICE is due to a simultaneous decrease in the first cycle irreversible capacity (shown in Fig. 8a) and increase in reversible capacity. The increase in reversible capacity indicates an increase in active Si

content. Therefore, annealing results in more stable oxygen sites and an increase in active Si content, which suggests disproportionation of SiO<sub>x</sub> into Si and SiO<sub>2</sub>, in agreement with the XPS results, discussed above. The linearity of Figs. 8a and 8b suggest that the extent of this disproportionation reaction is linear with temperature. This has indeed been observed to be the case by in situ IR measurements of SiO during heating.<sup>46</sup> The linear behavior of the disproportionation reaction with temperature being explained by a decreasing reaction rate as the reaction progresses.

Figure 9 shows the cycling performance of SiO<sub>x</sub> materials as a function of air exposure time during milling and annealing temperature. The cycling retention of SiO<sub>x</sub> synthesized here is improved with annealing temperature. Similar results for commercial SiO have been reported previously.<sup>33</sup> Samples milled in air for 8 h or greater have improved cycling performance that is comparable with the performance of commercial SiO. There is a significant improvement in cycling performance for all SiO<sub>x</sub> samples prepared with more than 4 h milling in air. This is coincident both with the suppression of Li<sub>15</sub>Si<sub>4</sub> formation (Fig. S8) and with the attainment of oxygen saturation during milling (Fig. S1). As discussed above, the oxygen saturated samples contain  $\leq 10$  nm active Si regions that are fully enclosed by a silicon oxide matrix. Such a microstructure is expected to be advantageous for good cycling performance, since Si aggregation is impeded during cycling and the active Si grains are protected from contact with the electrolyte. The differences in the microstructure observed between the heated samples and unheated samples are the removal of oxygen site defects, disproportionation of SiO<sub>x</sub>, and an increase in the average Si grain size. Of these, the removal of defects during heating may be the cause of improved cycling, since the defects may be associated with fractures created during ball milling. Therefore, the particles made by annealing may be less apt to fracture during cycling.

The capacity of the oxygen saturated samples prepared by our method is around 1500–2000 mAh g<sup>-1</sup> (or 1600–1800 Ah l<sup>-1</sup>), and is also much higher than that of the commercial SiO tested here ( $\sim 1000$  mAh g<sup>-1</sup> or 1400 Ah l<sup>-1</sup>). However, a major difference between the two is the small particle size and therefore high surface

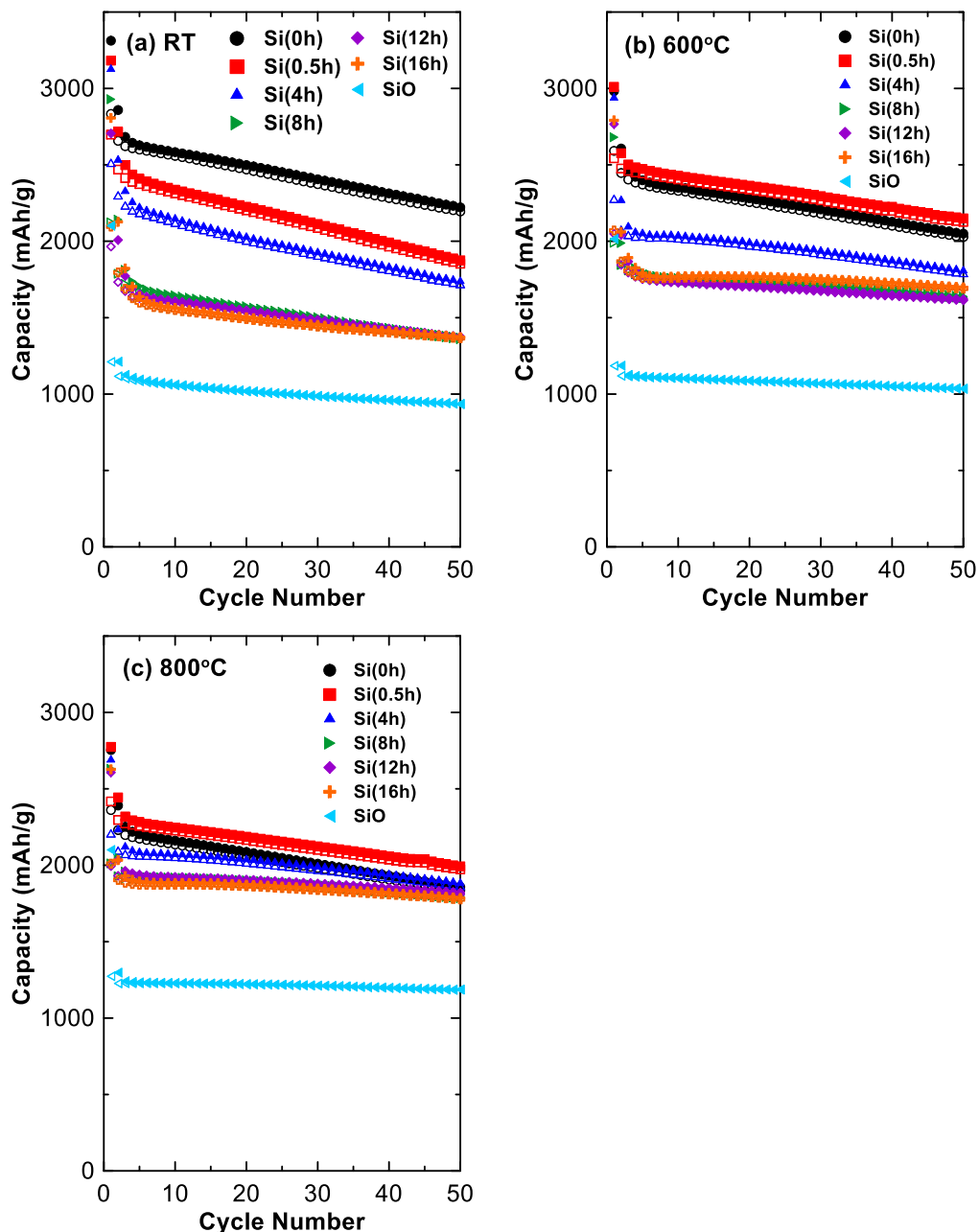


**Figure 9.** Cycling performance of (a) RT synthesized, (b) 600 °C annealed, and (c) 800 °C annealed SiO<sub>x</sub> electrodes. Sample compositions: Si(0h)-SiO<sub>0.08</sub>, Si(0.5h)-SiO<sub>0.12</sub>, Si(4h)-SiO<sub>0.21</sub>, Si(8h)-SiO<sub>0.37</sub>, Si(12h)-SiO<sub>0.37</sub>, Si(16h)-SiO<sub>0.37</sub>, SiO-SiO<sub>0.97</sub>.

area of the ball milled sample, which would result in higher surface reactivity with electrolyte during cycling. We are currently investigating methods to reduce the surface area of the ball milled samples and the effects of surface coatings in reducing reactivity.

### Conclusions

SiO<sub>x</sub> materials with various oxygen contents were synthesized by a simple room-temperature reactive gas milling method by controlling the air exposure time during milling. The resulting microstructure of the SiO<sub>x</sub> samples is that of n-Si and a-Si dispersed in an amorphous silicon oxide matrix. Si aggregation during high temperature treatment is effectively avoided, since  $\leq 10$  nm active Si regions are completely isolated by the amorphous matrix phase. A high potential capacity plateau occurs during the first lithiation and is related to defect oxygen sites and increases in potential and capacity as the oxygen content in SiO<sub>x</sub> is increased. During annealing, the

initial high potential oxygen plateau becomes smaller and reduces in potential as the defect sites are healed. The 1st irreversible capacity is attributed to the reaction of Li with oxygen in the suboxide matrix forming lithium silicate, and it is reduced in annealed samples also due to defect healing. As annealing temperature is increased, the ICE is increased from  $\sim 73\%$  to  $\sim 79\%$  and cycling performance improves. The capacity of the oxygen saturated samples synthesized here is around 1500–2000 mAh g<sup>-1</sup> (or 1600–1800 Ah l<sup>-1</sup>), which can be well maintained after high temperature annealing. With further improvements, SiO<sub>x</sub> materials made by reactive ball milling could be an attractive and likely less expensive alternative to conventionally made SiO.

### Acknowledgments

The authors would like to acknowledge funding from NSERC, Novonix Battery Testing Services, Inc. under the auspices of the

Industrial Research Chair program. We also acknowledge the support of the Canada Foundation for Innovation, the Atlantic Innovation Fund and other partners that fund the Facilities for Materials Characterization managed by the Institute for Research in Materials. We also would like to acknowledge Dr. Xiang Yang at Saint Mary's University for his assistance in acquiring SEM images, Dr. Jeff Dahn for use of pycnometer and BET surface area analyzer, Dr. J. Craig Bennett at Acadia University for his assistance in acquiring TEM images, and Dr. Andrew George for his assistance in acquiring XPS profiles. Dr. Yidan Cao acknowledges financial support from the Killam Trusts.

### ORCID

M. N. Obrovac  <https://orcid.org/0000-0001-5509-3185>

### References

1. M. Armand and J. M. Tarascon, *Nature*, **451**, 652 (2008).
2. J. B. Goodenough and Y. Kim, *Chem. Mater.*, **22**, 587 (2010).
3. Y. K. Jeong, T. W. Kwon, I. Lee, T. S. Kim, A. Coskun, and J. W. Choi, *Energy Environ. Sci.*, **8**, 1224 (2015).
4. J. Lopez, D. G. Mackanic, Y. Cui, and Z. Bao, *Nat. Rev. Mater.*, **4**, 312 (2019).
5. R. Weber, M. Genovese, A. J. Louli, S. Hames, C. Martin, I. G. Hill, and J. R. Dahn, *Nat. Energy*, **4**, 683 (2019).
6. A. Magasinski, P. Dixon, B. Hertzberg, A. Kvit, J. Ayala, and G. Yushin, *Nat. Mater.*, **9**, 353 (2010).
7. H. Kim, B. Han, J. Choo, and J. Cho, *Angew. Chemie*, **120**, 10305 (2008).
8. W. J. Zhang, *J. Power Sources*, **196**, 13 (2011).
9. M. N. Obrovac and L. Christensen, *Electrochem. Solid-State Lett.*, **7**, A93 (2004).
10. J. Yin, M. Wada, K. Yamamoto, Y. Kitano, S. Tanase, and T. Sakai, *J. Electrochem. Soc.*, **153**, A472 (2006).
11. M. N. Obrovac, *Curr. Opin. Electrochem.*, **9**, 8 (2019).
12. C. Gan, C. Zhang, W. Wen, Y. Liu, J. Chen, Q. Xie, and X. Luo, *ACS Appl. Mater. Interfaces*, **11**, 35809 (2019).
13. Z. Du, T. D. Hatchard, R. A. Dunlap, and M. N. Obrovac, *J. Electrochem. Soc.*, **162**, A1858 (2015).
14. U. Kasavajjula, C. Wang, and A. J. Appleby, *J. Power Sources*, **163**, 1003 (2007).
15. M. N. Obrovac and V. L. Chevrier, *Chem. Rev.*, **114**, 11444 (2014).
16. M. Li, J. Qiu, H. Ming, P. Zhao, Z. Jin, S. Zhang, and Y. Yang, *J. Alloys Compd.*, **809**, 151659 (2019).
17. M. L. Terranova, S. Orlanducci, E. Tamburri, V. Guglielmotti, and M. Rossi, *J. Power Sources*, **246**, 167 (2014).
18. K. L. Anh Cao, A. F. Arif, K. Kamikubo, T. Izawa, H. Iwasaki, and T. Ogi, *Langmuir*, **35**, 13681 (2019).
19. Y. Hwa, C.-M. Park, and H.-J. Sohn, *J. Power Sources*, **222**, 129 (2013).
20. J. Wang, H. Zhao, J. He, C. Wang, and J. Wang, *J. Power Sources*, **196**, 4811 (2011).
21. M. A. Al-Maghrabi, J. Suzuki, R. J. Sanderson, V. L. Chevrier, R. A. Dunlap, and J. R. Dahn, *J. Electrochem. Soc.*, **160**, A1587 (2013).
22. T. Morita and N. Takami, *J. Electrochem. Soc.*, **153**, A425 (2006).
23. M. Yamada, A. Ueda, K. Matsumoto, and T. Ohzuku, *J. Electrochem. Soc.*, **158**, A417 (2011).
24. A. Hirata, S. Kohara, T. Asada, M. Arao, C. Yogi, H. Imai, Y. Tan, T. Fujita, and M. Chen, *Nat. Commun.*, **7**, 1 (2016).
25. A. Hohl, T. Wieder, P. A. Van Aken, T. E. Weirich, G. Denninger, M. Vidal, S. Oswald, C. Deneke, J. Mayer, and H. Fuess, *J. Non. Cryst. Solids*, **320**, 255 (2003).
26. M. Nagamori, J.-A. Boivin, and A. Claveau, *J. Non. Cryst. Solids*, **189**, 270 (1995).
27. S. S. Suh, W. Y. Yoon, D. H. Kim, S. U. Kwon, J. H. Kim, Y. U. Kim, C. U. Jeong, Y. Y. Chan, S. H. Kang, and J. K. Lee, *Electrochim. Acta*, **148**, 111 (2014).
28. J. Hwang, K. Kim, W. S. Jung, H. Choi, and J. H. Kim, *J. Power Sources*, **436**, 226883 (2019).
29. M. Yamada, A. Inaba, A. Ueda, K. Matsumoto, T. Iwasaki, and T. Ohzuku, *J. Electrochem. Soc.*, **159**, A1630 (2012).
30. K. Kitada, O. Pecher, P. C. M. M. Magusin, M. F. Groh, R. S. Weatherup, and C. P. Grey, *J. Am. Chem. Soc.*, **141**, 7014 (2019).
31. X. Meng, H. Huo, Z. Cui, and X. Guo, *Electrochim. Acta*, **283**, 183 (2018).
32. M. Mamiya, M. Kikuchi, and H. Takei, *J. Cryst. Growth*, **237–239**, 1909 (2002).
33. C. M. Park, W. Choi, Y. Hwa, J. H. Kim, G. Jeong, and H. J. Sohn, *J. Mater. Chem.*, **20**, 4854 (2010).
34. G. Choi, J. Kim, and B. Kang, *Chem. Mater.*, **31**, 6097 (2019).
35. C. Guo, D. Wang, Q. Wang, B. Wang, and T. Liu, *Int. J. Electrochem. Sci.*, **7**, 8745 (2012).
36. N. Dimov, K. Fukuda, T. Umeno, S. Kugino, and M. Yoshio, *J. Power Sources*, **114**, 88 (2003).
37. F. Toschi, S. Orlanducci, V. Guglielmotti, I. Cianchetta, C. Magni, M. L. Terranova, M. Pasquali, E. Tamburri, R. Matassa, and M. Rossi, *Chem. Phys. Lett.*, **539–540**, 94 (2012).
38. C. Shen, R. Fu, H. Guo, Y. Wu, C. Fan, Y. Xia, and Z. Liu, *J. Alloys Compd.*, **783**, 128 (2019).
39. Y. S. Hu, R. Demir-Cakan, M. M. Titirici, J. O. Müller, R. Schlögl, M. Antonietti, and J. Maier, *Angew. Chemie - Int. Ed.*, **47**, 1645 (2008).
40. J. Zhang, P. Ma, Z. Hou, X. Zhang, and C. Li, *Energy Fuel*, **34**, 3895 (2020).
41. S. H. Ng, J. Wang, D. Wexler, S. Y. Chew, and H. K. Liu, *J. Phys. Chem. C*, **111**, 11131 (2007).
42. R. Huang, X. Fan, W. Shen, and J. Zhu, *Appl. Phys. Lett.*, **95**, 133119 (2009).
43. L. Chen, J. Zheng, S. Lin, S. Khan, J. Huang, S. Liu, Z. Chen, D. Wu, and R. Fu, *ACS Appl. Energy Mater.*, **3**, 3562 (2020).
44. Y. Cao, J. C. Bennett, R. A. Dunlap, and M. N. Obrovac, *Chem. Mater.*, **30**, 7418 (2018).
45. T. D. Hatchard, A. Genkin, and M. N. Obrovac, *AIP Adv.*, **7**, 045201 (2017).
46. B. J. Hinds, F. Wang, D. M. Wolfe, C. L. Hinkle, and G. Lucovsky, *J. Non. Cryst. Solids*, **227–230**, 507 (1998).